Materials Advances

ROYAL SOCIETY OF CHEMISTRY

PAPER

View Article Online
View Journal | View Issue



Cite this: *Mater. Adv.*, 2025, **6**, 9627

# Fabrication and the highly sensitive SERS performance of Ag-decorated ZnO flower-like microrods for methidathion detection

Nguyen Dac Dien,[a] Thi Thu Ha Pham,*[b] Xuan Hoa Vu,[c] Ngo Thi Lan,[c] Tran Thu Trang,[c] Pham Thi Nga,[cd] Pham The Chinh,[b] Truong Xuan Vuong,[b] Thi Thu Thuy Nguyen,[b] Cao Thanh Hai,[b] Tran Thi Kim Chi,[e] Tran Thi Huong Giang,[e] Pham Thanh Binh,[e] Nguyen Trong Nghia[f] and Nguyen Duc Toan[f]

Methidathion (MD), a highly hazardous pesticide, poses a severe threat to public health and the environment. This study presents a highly sensitive and reproducible surface-enhanced Raman scattering (SERS) substrate for the detection of trace amounts of MD. The substrate consists of silver nanoparticles (Ag NPs) embedded along the edges of hexagonal zinc oxide (ZnO) flower-like microrods (FLM), fabricated *via* a two-step process, namely, hydrothermal and chemical reduction methods. The structural, morphological, and optical characteristics of the prepared heterostructure were analyzed by scanning electron microscopy (SEM), transmission electron microscopy (TEM), high-resolution TEM (HRTEM), X-ray diffraction (XRD), energy-dispersive X-ray spectroscopy (EDS), EDX mapping, and UV-vis spectroscopy. The ZnO/Ag hybrid heterostructure exhibited superior SERS performance compared to the pure Ag and ZnO substrates. The SERS activity was systematically optimized by varying the Ag content, with ZnO/Ag4 demonstrating the highest enhancement factor (EF) of $1.1 \times 10^7$, a limit of detection (LOD) of 0.2 ppm and a wide linear range (0.2–20 ppm). The optimized substrate retained good activity after six months of preservation, confirming the stability of the SERS substrate. The improved SERS performance is attributed to the combined electromagnetic and chemical enhancement mechanisms, including a high density of plasmonic hotspots and efficient charge transfer at the ZnO/Ag interface. Density functional theory (DFT) simulation was employed to gain a deeper understanding of the electronic and vibrational modes contributing to the SERS enhancement. This work demonstrates the potential of the ZnO/Ag hybrid as a robust and effective SERS platform for the detection of hazardous chemicals in real-world agricultural samples.

Received 5th July 2025,
Accepted 20th October 2025

DOI: 10.1039/d5ma00710k

rsc.li/materials-advances



## 1. Introduction

Since its discovery 50 years ago, surface enhanced Raman scattering (SERS) has attracted considerable research interest in the scientific community,[1] including life science, biotechnology, homeland security, analytical chemistry, and food safety.[2,3] The analysis molecules are absorbed on the designed surface and reflect their characteristics in the SERS spectra. SERS is a sensitive vibrational spectroscopy technique and has been considered a powerful analytical method to detect organic dye molecules at low concentrations when they adsorb on metallic nanostructures owing to the plasmonic effect of the metallic surface.[4] A phenomenon called localized surface plasmonic resonance (LSPR) occurs in noble metal nanoparticles (NPs) such as silver (Ag), gold (Au), and platinum (Pt) when exposed to incident light.[5] Under laser irradiation, the surface plasmon of noble metal NPs tend to significantly enhance the evanescent field on the SERS substrate as a result of the LSPR in the visible to near infrared range.[5] The enhanced Raman signal will be generated from the analyte molecules in the vicinity of such a plasmonic field. However, noble metal NP-based SERS substrates have relatively low stability and cannot be reused

[a] *Faculty of Occupational Safety and Health, Vietnam Trade Union University, 169 Tay Son Street, Kim Lien Ward, Ha Noi City 10000, Vietnam*
[b] *Faculty of Chemistry, TNU-University of Sciences, Phan Dinh Phung Ward, Thai Nguyen Province 24000, Vietnam. E-mail: haptt@tnus.edu.vn*
[c] *Institute of Science and Technology, TNU-University of Sciences, Phan Dinh Phung Ward, Thai Nguyen Province 24000, Vietnam*
[d] *Faculty of Secondary School, Hoa Lu University, 2 Xuan Thanh Street, Hoa Lu Ward, Ninh Binh Province, Vietnam*
[e] *Institute of Materials Science, Vietnam Academy of Science and Technology, 18 Hoang Quoc Viet Road, Nghia Do Ward, Ha Noi City 10000, Vietnam*
[f] *Institute of Physics, Vietnam Academy of Science and Technology, 10 Dao Tan Street, Ngoc Ha Ward, Ha Noi City 10000, Vietnam*

owing to their easy agglomeration.[6] Recently, various heterostructures of semiconducting metal oxides (MOS) and plasmonic metal nanoparticles have been intensively investigated for SERS application owing to the synergistic effect between electromagnetic (EM) and charge transfer (CT) mechanisms.[7–9] The EM enhancement results from the LSPR of noble metal nanostructures, while the CT enhancement results from the charge transfer between SERS materials and target molecules. The hybridization of metal NPs with MOS has the advantages of a large surface area available for the formation of hotspots between closely neighboring nanoparticles and strong adsorption capability for target analytes.[10] Wu *et al.* designed a $BaTiO_3$/Ag NPs composite for improved SERS performance in detecting Rhodamine 6G (R6G).[11] This work demonstrated that the pyroelectric field generated by $BaTiO_3$ can effectively drive charge transfer, leading to a significant amplification of the SERS signal (70-fold improvement) and a reduction in the detection limit to $10^{-14}$ M. To bring SERS-based sensors to practical application, it is desirable that the SERS substrates based on a metal oxide semiconductor (MOS) and noble metal hybrid offer high sensitivity, good stability, as well as reproducibility towards organic pollutants.[8,12–14] Lin *et al.* successfully developed a hydrophobic CuO@Ag nanowire for trace nanoplastics by employing a novel approach based on the coffee ring effect.[15] Their work introduced a multiplex-feature analysis strategy that combines the SERS signal intensity with physical characteristics like the coffee ring diameter and the probability of detection (POD). By using a machine learning model to map these combined features to nanoplastic concentration, they achieved a remarkable 19-fold improvement in prediction accuracy compared to traditional methods.

Up to now, environmentally-friendly semiconductor materials with notable SERS properties ($Cu_2O$, ZnO, $TiO_2$, CuO, $Fe_2O_3$, *etc.*) have been used to efficiently detect organic pollutants.[16–20] However, the weak LSPR effect prevents semiconductor metal oxides from being used as SERS substrates to examine trace organic pollutants.[21] Zinc oxide (ZnO) nanostructures (nanotrees, nanorods, nanoplates, nanowires, nanoflowers, and nanotubes) have been widely explored for SERS substrates,[1,7,8,22] wherein the incorporation of ZnO with noble metals (Ag, Au, and Pt) can be used to prepare highly efficient SERS substrates due to the synergism between the EM mechanism of the noble metal and the charge-transfer (CT) process at the metal–semiconductor interface.[23,24] ZnO is rich in its morphological structure[25] and is a more inexpensive, biocompatible, chemically stable compared to other metal oxide semiconductors.[7] The noble metal/ZnO composite structures are ideal SERS substrates for detecting many organic substances such as Rhodamine B,[7] methylene blue,[8] malachite green,[26] dopamine,[27] 6-di-*t*-butyl-*p*-hydroxytoluene (BHT),[28] pesticide[29] and others.

Methidathion (MD) is an organic phosphorus-containing insecticide whose high toxicity is a serious threat to agricultural products and water.[30] This organic pollutant in trace amounts can accumulate in the food chain, which gives rise to the detrimental effect on human health. MD has been forbidden by the government, so it is particularly essential to develop a simple, rapid, and sensitive method to detect MD in fruits, vegetables, and wastewater. Consequently, the agriculture, food safety, medicine diagnosis and environment controlling fields consider the analysis of MD as an important research topic.[31] There are many methods that can be used to detect MD, including spectrophotometric analysis, catalytic reduction, UV or fluorescence spectroscopy, and high performance liquid chromatography (HPLC).[32–34] Although these techniques are sensitive, they involve complicated sample preparation steps, are time-consuming and expensive, and require skillful technicians.[32–34] The fluorescence method possesses high sensitivity but poor specificity and requires a long reaction time.[35,36] Compared with traditional techniques, SERS is an ultrasensitive detection technology even at the single molecule level[37,38] and is a cost-effective and time-saving approach.[39] Several SERS substrates have been prepared for MD detection. For example, Lin *et al.* showed that Ag NPs synthesized by the modified Tollens technique were deposited on glass slides for detecting the MD pesticide with a limit of detection (LOD) of 0.1 ppm.[40] Yao *et al.* reported the determination of MD in tea leaves by thin layer chromatography-SERS method with a limit of quantification (LOQ) of 0.1 ppm.[41] Cong Wang *et al.* prepared a SERS substrate based on Ag NPs-loaded chitosan foam to detect MD with a LOD at the μg level.[42] Additionally, these authors did not report the enhancement factors (EF) of their SERS substrates. To our best knowledge, there have not been any publications on ZnO/Ag for MD detection.

In this report, we fabricated a SERS substrate by decorating Ag NPs on ZnO flower-like microrods (FLM) by a two-step fabrication process, *i.e.*, hydrothermal and reduction route. The content of Ag was optimized by varying the amount of $AgNO_3$ added. Varied concentrations of methidathion (MD) as an analyte molecule were used to find the limit of detection (LOD) and enhancement factor (EF). A limit of detection (LOD) of 0.2 ppm and an enhancement factor (EF) of $1.1 \times 10^7$ were achieved. Additionally, the as-prepared ZnO/Ag substrate maintained excellent SERS performance after several cycles. Moreover, density functional theory (DFT) simulations were performed to identify the expected vibrational modes and electronic transitions. The obtained SERS substrate presented high sensitivity, good stability, homogeneity, and could detect trace amounts of methidathion.

## 2. Experimental section

### 2.1. Materials and chemicals

Zinc nitrate hexahydrate $Zn(NO_3)_2{\cdot}6H_2O$, potassium hydroxide (KOH), sodium hydroxide (NaOH), hydroxylamine ($NH_2OH$), silver nitrate ($AgNO_3$), methidathion ($C_6H_{11}N_2O_4PS_3$), and absolute ethanol ($C_2H_5OH$) were purchased from Merck Chemical Co. All the reagents used in this work were of analytical grade and used without further purification. Purified water was utilized in all experiments.

### 2.2. Fabrication of ZnO FLM

The fabrication of the ZnO flower-like microrods was performed using a method reported previously.[25] The chemical reaction between $Zn(NO_3)_2$ and KOH formed $Zn(OH)_2$ as follows:

$$Zn(NO_3)_2 + 2KOH \rightarrow Zn(OH)_2\downarrow + 2KNO_3 \quad (1)$$

$Zn(OH)_2$ molecules were transformed into ZnO and self-assembled into ZnO flower-like microrods under the hydrothermal conditions of 180 °C for 48 h:

$$Zn(OH)_2 \rightarrow ZnO + H_2O \quad (2)$$

Finally, the obtained product was removed from the solution, and rinsed with distilled water and absolute ethanol several times to remove the by-product $KNO_3$ and remnants to gain the ZnO FLM.

### 2.3. Preparation of Ag NPs

Ag NPs were prepared by chemical reduction using the $AgNO_3$ salt as a precursor of silver. 340 mg $AgNO_3$ solid salt was dissolved in 10 mL distilled water to give 0.2 M $AgNO_3$ solution. 0.5 mL of $AgNO_3$ solution (0.2 M) was added to 20 mL distilled water and heated to 60 °C, then 0.5 mL of NaOH solution (0.5 M) was added to the above $AgNO_3$ solution under continuous stirring to form the homogenous mixture. After that, 1 mL of $NH_2OH$ (0.2 M) was added dropwise to this mixture under stirring at 60 °C for 30 min. After stirring was turned off, the obtained solution was filtered, and washed with distilled water and absolute ethanol several times to remove the by-product $NaNO_3$ and remnants to gain Ag NPs:

$$3AgNO_3 + NH_2OH + 3NaOH \rightarrow 3Ag\downarrow + NO\uparrow + 3NaNO_3 + 3H_2O \quad (3)$$

### 2.4. Ag NPs decoration on ZnO FLM

Ag NPs were deposited on the ZnO FLM by chemical reduction method. 60 mg of the as-prepared ZnO FLM powder was dispersed in 20 mL of deionized water under stirring for 15 min. Then, five different volumes of 0.2 M $AgNO_3$ solution were added to the ZnO suspension under continuous stirring for 2 hours. After that, 0.5 mL of NaOH solution (0.5 M) was added dropwise, and the mixture was heated to 60 °C under continuous stirring for 30 min. Consequently, five corresponding volumes of $NH_2OH$ solution (0.2 M) were added dropwise into the above mixture while continuously stirring for 30 min. $AgNO_3$ was reduced by hydroxylamine to form metal silver, as shown in eqn (3). Table 1 shows the volumes of $AgNO_3$ solution (0.2 M), NaOH solution (0.5 M), and $NH_2OH$ (0.2 M) that were used to form the five ZnO/Ag samples named ZnO/Ag1, ZnO/Ag2, ZnO/Ag3, ZnO/Ag4, and ZnO/Ag5.

After stirring was turned off, the resultant yellow-brown colloidal solution appeared and was cooled to room temperature, filtrated and rinsed with purified water and absolute ethanol several times to remove the by-product ($NaNO_3$) and remnants, then dried at 80 °C overnight to obtain the ZnO FLM modified by Ag NPs. The content of Ag on the ZnO FLM plays a significant role in the SERS effect.

Table 1 Amounts of the precursors in the synthesis of ZnO/Ag

| Samples | $AgNO_3$ (0.2 M) | Ag:ZnO molar ratio | NaOH (0.5 M) | $NH_2OH$ (0.2 M) |
|---|---|---|---|---|
| ZnO/Ag1 | 0.1 mL | 0.0432 | 0.5 mL | 0.2 mL |
| ZnO/Ag2 | 0.25 mL | 0.108 | | 0.5 mL |
| ZnO/Ag3 | 0.5 mL | 0.216 | | 1 mL |
| ZnO/Ag4 | 0.75 mL | 0.324 | | 1.5 mL |
| ZnO/Ag5 | 1 mL | 0.432 | | 2 mL |

### 2.5. Fabrication of the SERS substrate

Fig. 1(a) illustrates the fabrication procedure for the SERS substrate and the SERS detection process. The process mainly involves three steps. First, a glass plate of 1 cm × 1 cm in size was thoroughly washed and ultrasonically cleaned by distilled water to remove any organic residue from the surface, and then dried in air at 80 °C. Second, the pure Ag NPs, pristine ZnO FLM or ZnO/Ag hybrids were then deposited onto the glass slide using the drop process. Here, 10 mg Ag, ZnO or ZnO/Ag powders were dispersed in 2 mL distilled water, and a 20 μL suspension was drop-casted onto the clean glass plate and dried at room temperature to be applied as the SERS substrate. MD was selected as the probe molecule for SERS measurement. The MD solutions were prepared in different concentrations (0.2–20 ppm) through dissolving MD in various volumes of distilled water. Finally, these SERS substrates were immersed in MD solutions for 20 min to reach the MD adsorption equilibrium on the Ag, ZnO, or ZnO/Ag surface. After being taken out, the SERS substrates were left to dry at room temperature so that the MD molecules were evenly distributed on the solid surface after solvent evaporation. The chemical structure of the MD molecule is shown in Fig. 1(b and c).

### 2.6. Characterization

The as-prepared Ag NPs, ZnO FLM, and ZnO/Ag hybrids were observed under scanning electron microscopy (SEM, Hitachi S4800, Japan) and transmission electron microscopy (TEM, Philips CM-200, Japan) to confirm the morphology, size, gap between nanoparticles, and the adhesion of Ag NPs to the ZnO FLM. High-resolution transmission electron microscopy (HRTEM) was performed using a JEM-2100F (Japan). The crystalline structure of the as-fabricated products were characterized using an X-ray diffractometer (XRD, Bruker D8 Advance, Germany) with Cu-$K_\alpha$ radiation (X-ray wavelength of $\lambda$ = 1.5406 Å). The diffractometer was operated at an accelerating voltage of 45 kV and anode current of 40 mA. Elemental quantification was performed on an energy-dispersive X-ray spectrophotometer (EDS, Hitachi SU 8020, Japan) operating at an accelerating voltage of 200 kV. Elemental mapping analysis was carried out on a Zeiss GeminiSEM 500 to verify the presence of Ag, Zn, and O elements in the samples. The ultraviolet-visible (UV-vis) absorption spectra were recorded on a JASCO V-770 spectrophotometer in the 300–800 nm wavelength range to measure the surface plasmon resonance

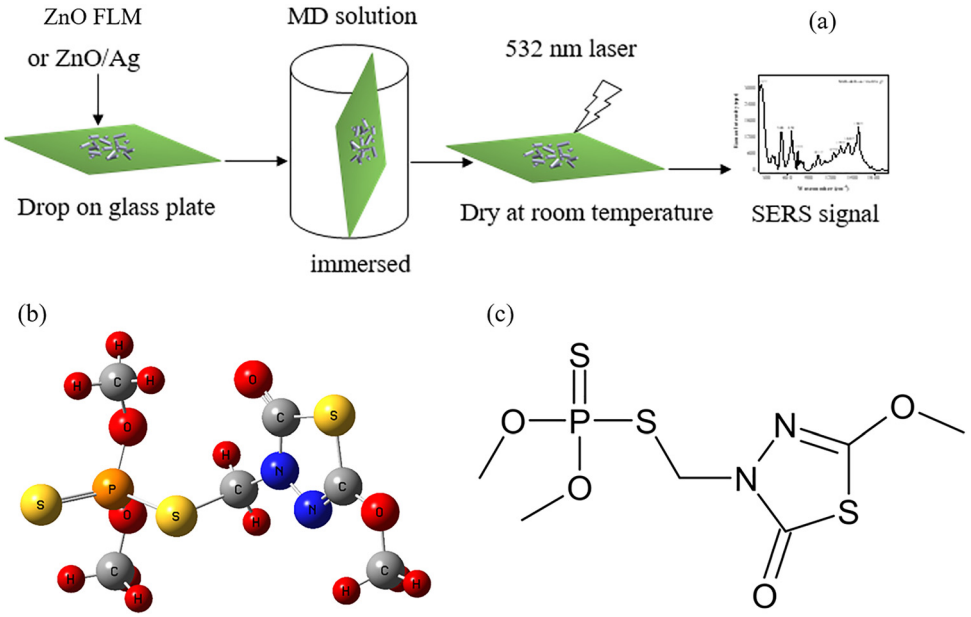


Fig. 1 (a) The preparation of the SERS substrate and SERS detection process, (b) space distribution of atoms in the MD molecule, (c) chemical structure of the MD molecule.

absorption spectra. The photoluminescence (PL) spectra were obtained using a fluorescence spectrometer (FLS1000, UK). The Raman measurements were obtained at room temperature using a Raman spectrometer (Horiba Xplora plus Raman microprobe, France) equipped with a 532 nm line laser as excitation and 50× objective. The laser spot area was ~1 μm in diameter and the incident power was 3.2 mW. The integration time of all spectral acquisitions for each measurement was set to be 10 s and was the same for all of the Raman spectra. 10 random spots on the same ZnO/Ag4 substrate were examined to confirm the homogeneity.

### 2.7. Computational details

The density functional theory (DFT) calculations were performed in the Gaussian 09 program to search the ground-state geometries of methidathion. The molecular structure was guessed using the B97D functional in conjunction with the cc-pVTZ basis set. The convergence threshold parameters were set as follows: $2 \times 10^{-5}$ Hartree for the energy and $5 \times 10^{-3}$ Angstrom for displacement. Then, the Raman spectrum of MD at the ground state was calculated at the same level of theory. The electronic structure of the global minima MD was explored using spin multiplicities and molecular orbitals. To confirm our optimization as the global minimum structure, harmonic vibrational frequencies were investigated.

## 3. Results and discussion

### 3.1. Characterization

Fig. 2 depicts the SEM images of the as-synthesized ZnO FLM and ZnO/Ag composites. Fig. 2(a and b) shows the surface morphology of the ZnO FLM with the hexagonal cross-section, an average length of approximately 20 μm, diameter of 1 μm, and uniform growth along the *c*-direction. As shown in Fig. 2(c–g), the SEM images primarily provide an initial overview of the surface morphology and the presence of Ag nanoparticles within the composite. It can be seen that Ag NPs are successfully deposited onto the surface of the ZnO FLM and the amount of Ag NPs on the ZnO FLM can be controlled by adjusting the volume of the $AgNO_3$ solution. As shown in Fig. 2c, few Ag NPs are anchored on the ZnO FLM surface in the ZnO/Ag1 sample. The large nanogaps between Ag NPs in the ZnO/Ag1 prevent the creation of a high-density hotspot. In the ZnO/Ag2 sample, the Ag NPs are deposited more densely on the ZnO FLM surface (Fig. 2d), and the density of Ag NPs on ZnO/Ag3 (Fig. 2e) is higher than that on ZnO/Ag1 and ZnO/Ag2. The nanogaps between the Ag NPs could contribute considerably to the SERS effect. The smaller nanogaps in ZnO/Ag4 (Fig. 2f) help to form more hotspots and improve the SERS signals. However, in ZnO/Ag5, excessive Ag NPs are anchored on the ZnO FLM, and neighboring Ag NPs are heaped together and wrapped around the ZnO FLM surface (Fig. 2g). The noticeable nanoparticle agglomeration leads to the formation of nanoparticle clusters. The agglomeration phenomenon results in the reduction of the gaps between Ag NPs, which reduces the SERS performance.

Fig. 3a shows the TEM image of the as-synthesized Ag NPs with good dispersity and good uniformity. The morphology of Ag NPs is quasi-spherical with an average diameter of approximately 20 nm. As shown by the TEM image of ZnO/Ag4 in Fig. 3b, Ag NPs are anchored on the surface of ZnO FLM with the gap between the two nearest-neighbor Ag NPs within the range of 50–100 nm to accommodate the hotspot locations. The effective surface area of ZnO/Ag is larger than that of pristine ZnO FLM. Thus, the analytic molecules have more space to interact with the hotspot sites in the substrate surface to give

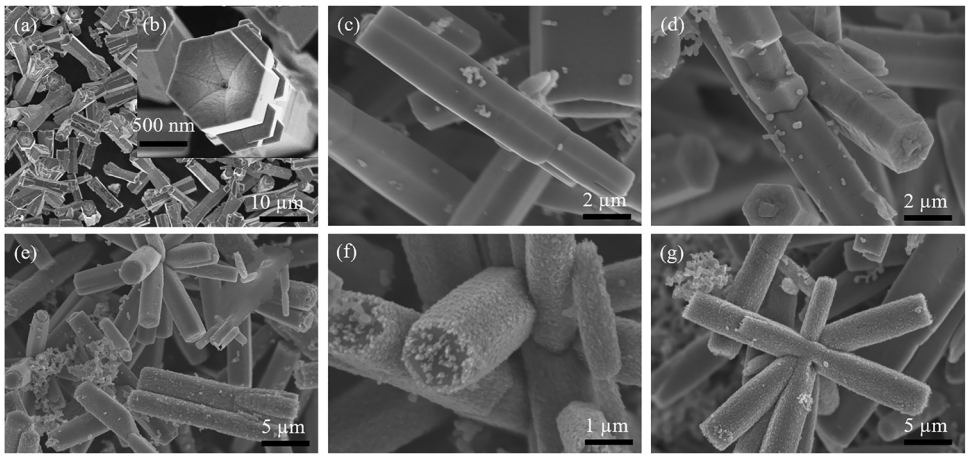


Fig. 2 SEM images of the (a and b) ZnO FLM, (c) ZnO/Ag1, (d) ZnO/Ag2, (e) ZnO/Ag3, (f) ZnO/Ag4, and (g) ZnO/Ag5.

greater overall Raman signal enhancement. The Ag NPs microstructure was analyzed in more detail utilizing HRTEM (Fig. 3c). The (111) lattice spacing of 0.234 nm can be observed, verifying the crystal nature of Ag with the face-centered-cubic structure.[43] EDS analysis was performed to confirm the creation of the ZnO/Ag4 composite, as shown in Fig. 3e. Both Ag and Zn can be observed in the spectrum. The weight percentages for Ag, Zn, and O are measured as 42.69, 39.94, and 17.37, respectively.

The ZnO/Ag4 composite microstructure was analyzed in more detail using scanning TEM. As shown in Fig. 4(a and b), a large amount of Ag NPs was deposited on the surface of the ZnO FLM with a particle size of approximately 20 nm. The ZnO/Ag interface offers the possibility of charge transfer, contributing to the enhanced Raman signal. EDX mapping confirms the presence of Zn, O, and Ag, with Ag elements distributed on ZnO FLM, as shown in Fig. 4(c–e). The distribution of Ag, Zn, and O in the ZnO/Ag4 sample was measured by elemental mapping for Ag (yellow), Zn (light green), and O (red). It clearly shows that Zn and O have larger densities than Ag. The elemental mapping reveals the high purity and uniformity of the sample, representing the successful synthesis of the ZnO/Ag composite structure.

### 3.2. Structural characterization

Information on the crystal structure of the prepared samples was obtained using XRD. Fig. 5a shows the XRD patterns of the Ag, ZnO, ZnO/Ag hybrid nanostructures. The crystal phase of ZnO marked with "!" and the peaks of Ag marked with "*" can be seen in Fig. 5a. The peak positions of pure ZnO at 31.7°, 34.3°, 36.2°, 47.4°, 56.5°, 62.8°, 66.3°, 67.8°, 69.0°, 72.5°, and 76.8° correspond to the (100), (002), (101), (102), (110), (103), (200), (112), (201), (004), and (202) planes, respectively, of the ZnO hexagonal wurtzite structure (JCPDS card no. 36-1451).[44] The diffraction peaks of ZnO FLM are sharp, showing that ZnO FLM has high crystallinity. The peaks at 37.9°, 44.1°, 63.9°, and 76.7° correspond to the (111), (200), (220), and (311) planes, respectively, of Ag NPs face-centered cubic (FCC) structure

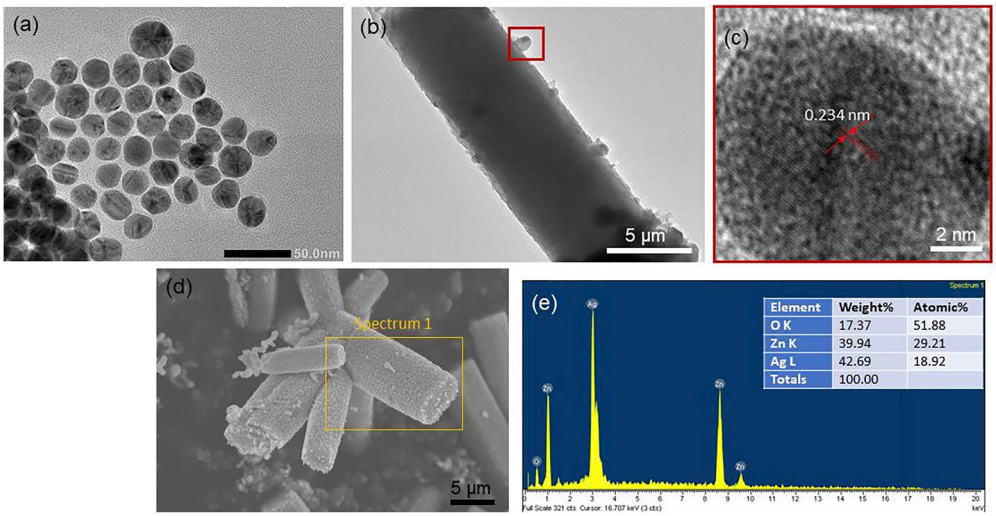


Fig. 3 TEM images of the (a) Ag NPs and (b) ZnO/Ag4, (c) HRTEM image of the Ag NPs, (d) SEM image and (e) EDS spectrum of ZnO/Ag4.

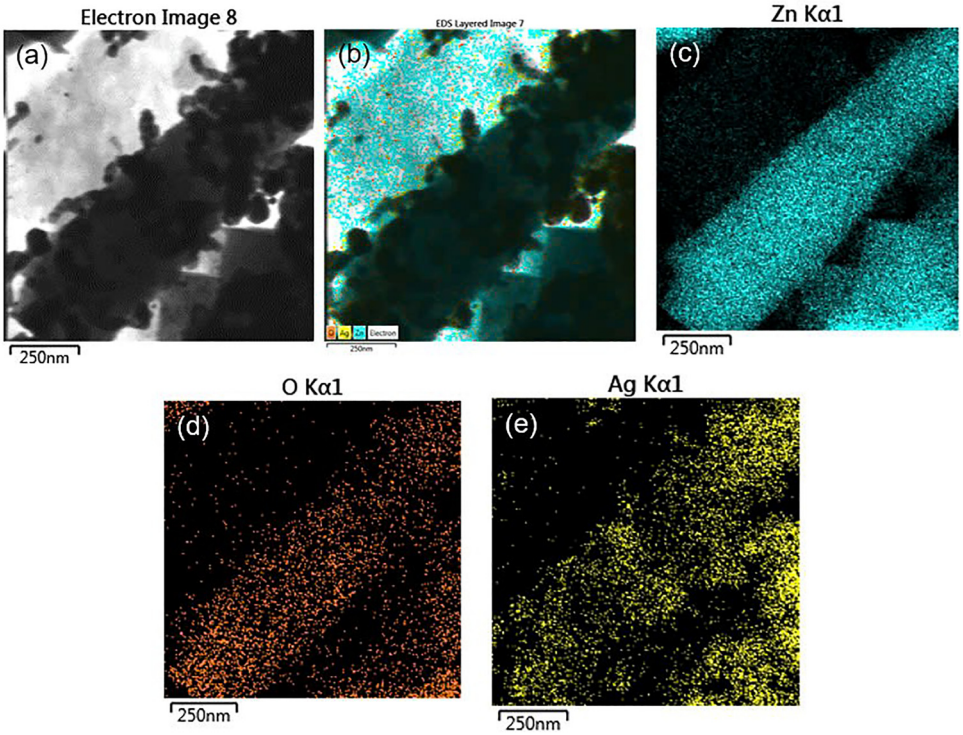


Fig. 4 (a) and (b) Scanning TEM and (c)–(e) EDX mappings of Zn, O, and Ag of the ZnO/Ag4 sample.

(JCPDS card no. 04-0783).[7] For the ZnO/Ag hybrid, besides the peaks of ZnO, we can see the diffraction peaks of Ag. No other peaks are observed, proving that ZnO/Ag has high purity during the preparation process. In addition, the peak intensity of the Ag NPs increased as the amount of Ag was increased from ZnO/Ag1 to ZnO/Ag5 (Fig. 5a).

The crystallite sizes were calculated from the (111) diffraction peak for Ag and from the (100) peak for other samples, using the Scherrer equation as shown in Fig. 5b:[45]

$$D = \frac{k\lambda}{\beta \cos\theta} \quad (4)$$

where $D$ is the crystalline size, $k$ = 0.893 is the Scherrer constant, $\lambda$ = 0.15406 nm is the wavelength of the X-ray, $\beta$ is the full width at half maximum of the diffraction peak (rad), and $\theta$ is the Bragg's diffraction angle. The average crystalline sizes of Ag NPs, ZnO, ZnO/Ag1, ZnO/Ag2, ZnO/Ag3, ZnO/Ag4, and ZnO/Ag5 were 20, 28, 38, 41, 34, 33, and 80 nm, respectively. Small, spherical Ag NPs were uniformly distributed on the ZnO FLM surface, and the crystalline size was dependent on the Ag content. The minimum size was achieved at ZnO/Ag4 (Fig. 5b). These results confirmed the successful synthesis of the ZnO/Ag composite.

### 3.3. PL and UV-vis spectra of ZnO and ZnO/Ag

To analyze the LSPR activity of ZnO and ZnO/Ag, the extinction photoluminescence (PL) was studied. Fig. 6a shows the PL

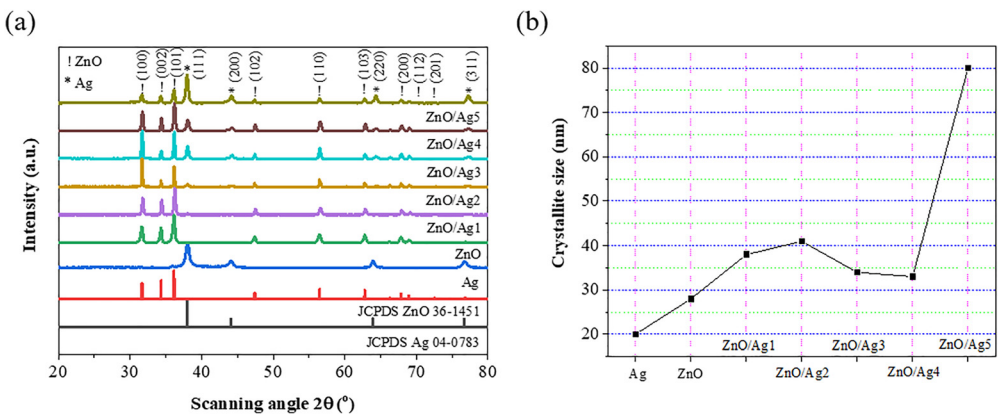


Fig. 5 (a) X-ray diffraction patterns of the Ag, ZnO and ZnO/Ag hybrid heterostructures and (b) the corresponding crystal sizes calculated from the Scherrer equation.

spectra of ZnO and ZnO/Ag with various Ag amounts and presents an intense emission peak at 384 nm for both ZnO and ZnO/Ag. A broad peak appears at 650 nm due to the presence of ZnO. The intensity of this peak decreases with the rise of Ag content from ZnO to ZnO/Ag5.

To analyze the optical absorption and the LSPR activity of Ag NPs, ZnO FLM, and ZnO/Ag of different contents, the extinction behavior was studied within the wavelength range of 300–800 nm. A singular strong absorption peak emerges at around 400 nm of Ag spherical nanoparticles of size 20 nm, as depicted in Fig. 6b.[40]

The absorption behavior of ZnO/Ag exhibits a basic absorption edge of ZnO FLM, along with a wide absorption edge between 400 and 500 nm that can be attributed to the surface plasmon resonance (SPR) of the Ag metallic nanoparticles.[46] The UV-vis absorption properties confirm the formation of plasmonic Ag NPs on the surface of the ZnO FLM *via* chemical reduction. When the Ag content increases from ZnO/Ag1 to ZnO/Ag5, the LSPR peak position undergoes a slight blue-shift towards higher energies (from 470 nm to 430 nm) (Fig. 6c), while the value of the extinction cross-section increases. The observed blue-shift of the absorption peak with increasing Ag amount can be attributed to the decreasing refractive index of the surrounding medium, the decreasing separation between Ag NPs, and the enhanced coupling effect between the two nanoparticles.[22] Fig. 6d shows the Tauc plots of the ZnO FLM and ZnO/Ag samples. The bandgap energy ($E_g$) of semiconductors can be calculated from Tauc's equation:[47]

$$(\alpha h\nu)^2 = A(h\nu - E_g) \quad (5)$$

Here, $\alpha$ is the absorption coefficient of the materials, $h$ is Planck constant, $\nu$ is the light frequency, $h\nu$ is the photon energy of the exciting light, and $A$ is a constant.

ZnO is a well-known direct bandgap semiconductor (bandgap of 3.2–3.4 eV corresponding to a direct allowed transition). The Tauc plot is the function of $(\alpha h\nu)^2$ along the vertical axis against the photon energy ($h\nu$) in eV along the horizontal axis. The linear extrapolation of the $(\alpha h\nu)^2$ *versus* $h\nu$ plot yields a straight-line region, and the intercept of the tangent of the linear region with the energy axis gives the optical bandgap energy ($E_g$) of the samples. The bandgap energies of the pristine ZnO, ZnO/Ag1, ZnO/Ag2, ZnO/Ag3, ZnO/Ag4, ZnO/Ag5 hybrid structures were 3.15, 3.1, 3, 2.95, 2.9, and 2.85 eV, respectively. It can be seen that the bandgap energy decreases with increasing Ag amount on the ZnO surface (inset of Fig. 6d). These results are consistent with previous literature reports.[21,27,48] Thanks to the low bandgap of ~2.9 eV, ZnO/Ag4 is brought closer to the excitation laser energy (532 nm), which facilitates the charge-transfer resonance between the substrate and analyte molecules. This alignment might significantly promote the chemical enhancement mechanism, working together with the

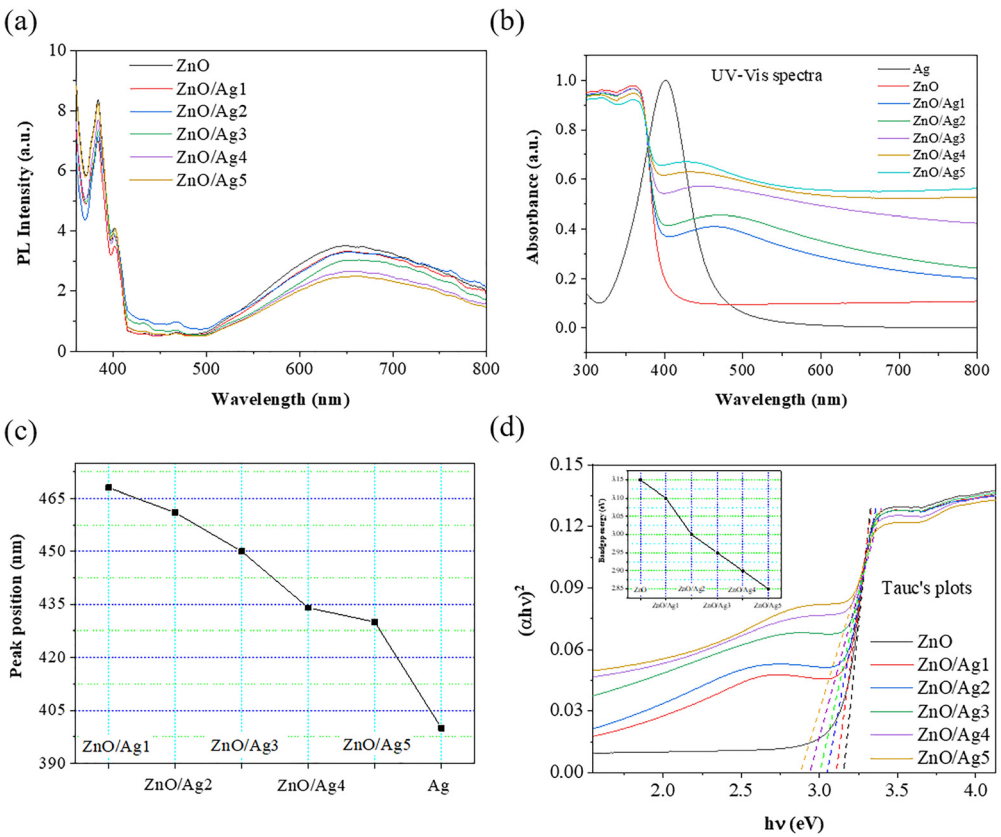


Fig. 6 (a) PL spectra of ZnO and ZnO/Ag, (b) UV-vis spectra of the Ag NPs, ZnO FLM and ZnO/Ag hybrids, (c) absorption peak position of the Ag and ZnO/Ag samples, and (d) Tauc plot of the ZnO FLM and ZnO/Ag samples, with the inset shows the bandgap energy of ZnO and ZnO/Ag.

plasmonic effect to achieve superior sensitivity. Therefore, ZnO/Ag4 is chosen for the SERS study to detect MD.

### 3.4. Raman spectra of MD on a glass substrate and ZnO/Ag4

Our experimental results showed that the ZnO/Ag heterostructure is favorable to SERS application in the detection of a low concentration of MD molecules. Ag NPs exhibit plasmonic nature under the simulated source of 532 nm close to the surface of the ZnO FLM, leading to the electromagnetic enhancement of SERS signals of MD molecules. This increase in the plasmonic behavior can be ascribed to multiple hotspots in close proximity between Ag NPs and ZnO FLM. The one-dimensional structure of the ZnO FLM facilitates the formation of hotspot regions and a large surface area to accommodate MD molecules in the vicinity of the hotspots. The incident photons are absorbed on the surface of the active plasmonic materials. When combined, these features significantly improve the SERS performance of this heterostructure.

In order to apply the Raman spectrum of MD in the real samples in the future, we calculated the Raman spectrum by DFT method and compared it to the experimental result from MD on glass in the wavenumber range of 300–2000 $cm^{-1}$ (Fig. 7). Major peaks appearing at 510, 653, 745, 1020, 1244, 1448, and 1583 $cm^{-1}$ correspond to various vibrational modes of the MD molecules, as shown in Table 2. A strong band at 510 $cm^{-1}$ corresponds to the scissoring of the C–S–C bond. The band at 745 $cm^{-1}$ corresponds to the twisting of the C═N–N bond. The most important difference between the calculated and experimental Raman spectra lies in the symmetricity of the S atom in the MD molecular structure. In the DFT calculations, the isolated MD molecule was optimized under vacuum without considering intermolecular interactions or substrate effects. In contrast, the experimental spectrum was obtained for MD adsorbed on a glass substrate (and later on a ZnO/Ag substrate), where the intermolecular hydrogen bonding, orientation, and surface–molecule charge transfer can lead to shifts in the vibrational frequencies. The noticeable variations in the peak positions and relative intensities between the two Raman spectra can be easily distinguished from Fig. 7. Actually, both calculated and experimental spectra show 653 and 1583 $cm^{-1}$ peaks corresponding to the stretching of N–C–S and S–C–N bonds, respectively. In addition to these modes, the experimental Raman spectrum shows additional modes at 1020, 1244, and 1448 $cm^{-1}$ corresponding to the stretching of C–O–P and S–P═S vibrational modes, and the scissoring of the O–C–O bond, respectively, which are absent in the calculated one.[49]

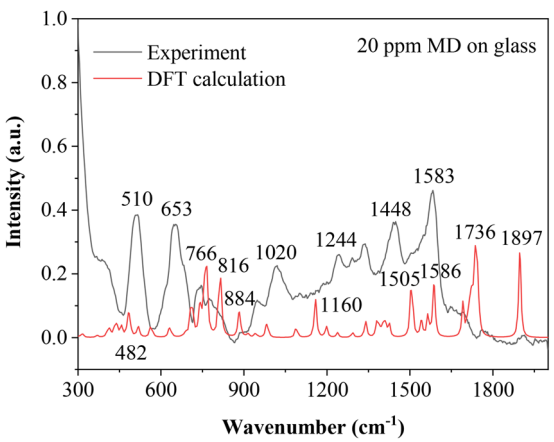


Fig. 7 Raman spectra of 20 ppm MD on a glass substrate (experiment) and calculated by DFT.

Table 2 The experimentally observed and DFT calculated frequencies of the skeletal vibration for MD and the corresponding vibration modes

| Experimental Raman peak ($cm^{-1}$) | DFT calculation ($cm^{-1}$) | Mode descriptions | Vibration modes |
|---|---|---|---|
| | 482 | O–P–O | Stretching |
| 510 | | C–S–C | Scissoring |
| 653 | 650 | N–C–S | Stretching |
| 745 | 766 | C═N–N | Twisting |
| | 816 | C═C | Stretching |
| | 884 | O–P–O | Scissoring |
| 1020 | | C–O–P | Stretching |
| 1244 | | S–P═S | Stretching |
| 1448 | | O–C–O | Scissoring |
| | 1505 | C–H | Stretching |
| 1583 | 1586 | S–C–N | Stretching |
| | 1736 | C═N | Stretching |
| | 1897 | C–N | Stretching |

### 3.5. SERS performance towards methidathion (MD)

Sensitivity, linearity, homogeneity, and stability are major concerns for any SERS substrates. To evaluate the SERS activity of the ZnO/Ag hybrid substrates, we measured the Raman spectra of MD molecules adsorbed on 8 samples: glass, pristine Ag NPs, bare ZnO FLM, ZnO/Ag1, ZnO/Ag2, ZnO/Ag3, ZnO/Ag4, and ZnO/Ag5 on a glass plate. In this study, we prepared MD solutions with different concentration gradients from 0.2 to 20 ppm. Fig. 8a shows the comparison between the Raman spectrum from 20 ppm MD on a glass plate and the SERS spectra of pristine Ag NPs, pure ZnO FLM and ZnO/Ag hybrids towards the same concentration of MD. The SERS spectrum measured on the pristine Ag substrate shows the characteristic peaks of MD at 504, 650, 736, 1017, 1239, 1330, 1437, and 1583 $cm^{-1}$ due to the LSPR effect of Ag in visible light. It can be observed that, compared with pure ZnO and Ag substrates, ZnO/Ag hybrids exhibit better Raman enhancement. Three characteristic peaks from the MD adsorbed on ZnO/Ag substrates located at 504, 650, and 1583 $cm^{-1}$ are notably enhanced. It is evident from the Raman spectra that with the increase of the Ag loading, the SERS intensity of the MD molecule shows a trend of first increasing and then decreasing, and the enhancement of the Raman signals of MD reached a maximum in ZnO/Ag4 (Fig. 8c). The result showed that an Ag:ZnO ratio of 0.324 was the optimal condition for the preparation of the ZnO/Ag SERS substrate. The Raman signal gradually decreased as the Ag : ZnO ratio deviated from the optimal value. It suggested that the hotspots field-enhancement is brought by the ZnO–Ag heterojunction interface. The electric field strength increases as the gap between the Ag NPs decreases from ZnO/Ag1 to ZnO/Ag4 under 532 nm

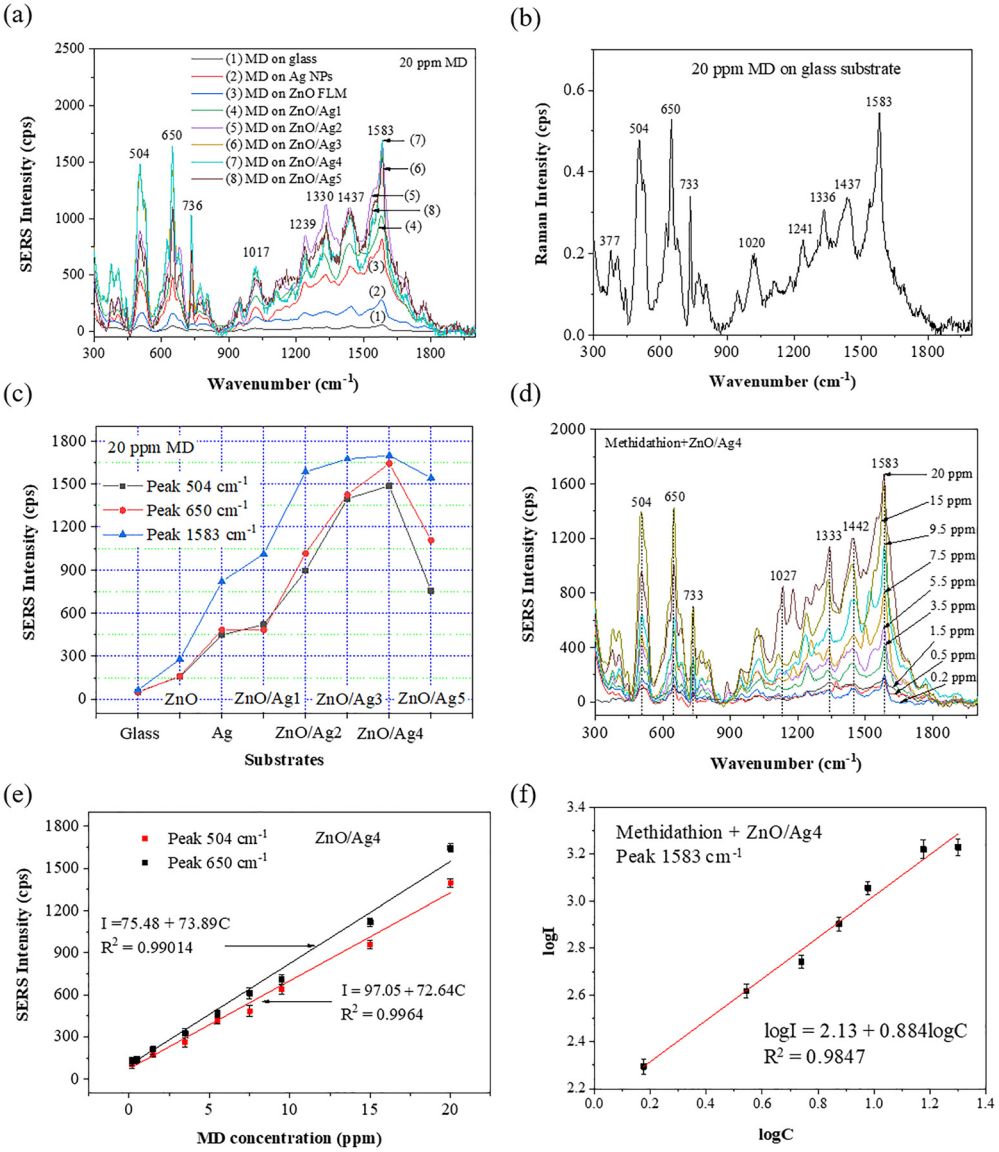


Fig. 8 (a) SERS performance comparison between Ag, ZnO, and ZnO/Ag with 20 ppm MD; (b) Raman spectrum of 20 ppm MD on a glass plate; (c) SERS intensities of the 504, 650, and 1583 $cm^{-1}$ peaks with 20 ppm MD as a function of the Ag content in ZnO/Ag hybrids; (d) SERS spectra of MD at various concentrations (0.2–20 ppm) on the ZnO/Ag4 substrate; (e) the linear relationship between the SERS intensities of 504 $cm^{-1}$ and 650 $cm^{-1}$ peaks and the MD concentration; and (f) the linear relationship between the logarithm of the 1583 $cm^{-1}$ peak intensity and the logarithm of the MD concentration (0.2–20 ppm).

laser irradiation. However, the electric field strength decreases as the gap between the Ag NPs further decreases from ZnO/Ag4 to ZnO/Ag5, leading to the decrease of the Raman signal.

Such an improvement suggests that the ZnO/Ag heterostructure plays an essential role in the SERS enhancement. ZnO/Ag4 is chosen as the optimal SERS material for the following investigation. Fig. 8d shows the SERS performance of ZnO/Ag4 with varied concentrations of MD molecules (0.2–20 ppm). It can be inferred that even at a low concentration of MD (0.2 ppm), the peaks at 504, 650, and 1583 $cm^{-1}$ were still observed. The Raman fingerprint signal of the MD molecules ceased to appear when the MD concentration was lower than 0.2 ppm. The background signal has no significant effect on the line, so it can be considered that 0.2 ppm ($2 \times 10^{-9}$ M) was the limit of detection (LOD) of the MD solution, which is lower than the allowable residue standard ($10^{-5}$ M). With the increase in the concentration, the Raman signal strength of the MD molecules gradually changes. The peak intensifying at 504 $cm^{-1}$ is ascribed to the interaction of MD molecules with the SERS materials. Moreover, the results showed a good linear relationship between the peak intensities at 504 $cm^{-1}$ and 650 $cm^{-1}$ and the MD concentration in the range of 0.2–20 ppm (Fig. 8e). For the 504 $cm^{-1}$ peak, the linear regression equation is $I$ = 97.05 + 72.64$C$ and the correlation coefficient $R^2$ is 0.9964. For the 650 $cm^{-1}$ peak, the linear regression equation is $I$ = 75.48 + 73.89$C$ and the correlation coefficient $R^2$ is 0.99014. For the 1583 $cm^{-1}$ peak (Fig. 8f), the

linear regression equation between the logarithm of the peak intensity and logarithm of the MD concentration (0.2–20 ppm) is $\log I = 2.13 + 0.884 \log C$ and the correlation coefficient $R^2$ is 0.9847.

Table 3 shows the comparison of the MD detection limit of the ZnO/Ag heterostructure with similar SERS substrates. Although the detection limit of ZnO/Ag (0.2 ppm) is slightly higher than those reported for the colloidal Ag and Au substrates, the hybrid structure offers significant advantages in terms of reproducibility, long-term stability, and ease of preparation. These considerations highlight the practical potential of ZnO/Ag hybrids despite their moderate detection limit compared to colloidal systems.

The two highest peaks at 504 and 1583 $cm^{-1}$ were used as the characteristic peaks for MD sensitive identification. The enhancement factor (EF) is an essential parameter for quantifying the performance of the SERS substrate and is estimated according to the following equation:[9]

$$EF = \frac{I_{SERS}}{I_{nor}} \times \frac{C_{nor}}{C_{SERS}} \quad (6)$$

Here, $I_{SERS}$ denotes the SERS intensity of MD on ZnO/Ag4, $I_{nor}$ is the Raman intensity of MD on a glass substrate without the SERS effect, $C_{SERS}$ is the MD concentration (0.2–20 ppm), and $C_{nor}$ = 302 320 ppm is the MD concentration on the glass substrate. EF of the ZnO/Ag4 substrate was calculated from a reference Raman spectrum of MD and the acquired SERS spectra. The reference Raman spectrum of the MD molecules was obtained on a glass substrate and the SERS spectra were acquired on ZnO/Ag4 under identical conditions. The maximum enhancement factor for MD at 504 and 1583 $cm^{-1}$ was computed to be $7.4 \times 10^6$ and $1.1 \times 10^7$, respectively, when the MD concentration was 0.2 ppm.

Good uniformity is one of the essential parameters for the practical application of the SERS substrate. To determine the uniformity of the ZnO/Ag4 substrate, SERS spectra of MD molecules with a concentration of 1.5 ppm from 10 randomly selected places on the ZnO/Ag4 substrate were collected under identical experimental conditions. As shown in Fig. 9a, the Raman spectra of MD indicate the reproducibility of the ZnO/Ag4 substrate. However, there are still slight fluctuations in the peak intensities, which may be due to the non-uniform adsorption of Ag NPs and MD molecules. The homogeneity of the SERS signal is evaluated through the relative standard deviation (RSD) of the 1583 $cm^{-1}$ peak strength. The RSD value is 9.36%, as shown in Fig. 9c, indicating the good uniformity of the substrate and favoring reproducible SERS signals from diverse spots. The strategy of submerging SERS substrates into MD solution can prevent the MD molecules in the solution from being deposited at the edges and inhibiting the coffee ring effect, improving the homogeneity of the SERS substrates.

Table 3 Comparison on the SERS performance of several substrates for the MD molecule

| Materials | Detection limit | EF | Ref. |
|---|---|---|---|
| Ag NPs | 0.1 ppm | Not reported | 40 |
| Au NPs | 0.1 ppm | Not reported | 41 |
| Ag NPs–chitosan | μg level | Not reported | 42 |
| ZnO/Ag | 0.2 ppm | $1.1 \times 10^7$ | This work |

Fig. 9b shows the SERS spectra from five independently prepared ZnO/Ag4 substrates, and Fig. 9d shows that the RSD value is 8%, which demonstrates the uniformity and reproducibility across different substrates. It can be observed from Fig. 9e that the strong peaks at 504, 650, and 1583 $cm^{-1}$ can be recognized at MD concentrations as low as 0.2 ppm, which shows the excellent performance of the ZnO/Ag4 substrate. To test the long-term stability of the ZnO/Ag4 substrate, SERS spectra of 0.2 ppm MD adsorbed on the same substrate were detected after 6 months of preservation.

No substantial change was observed in the SERS spectra after a 6-month period of aging, indicating that the ZnO/Ag4 substrate has excellent stability and can be stored at room temperature for long periods. This shows that the ZnO/Ag substrate retained its SERS activity even after six months of storage, which is rarely achieved with colloidal systems that often suffer from aggregation and instability. Such robustness makes the ZnO/Ag hybrid more practical for real-world sensing applications, where durability and consistency are critical factors.

### 3.6. Mechanism of SERS detection

SERS performance is usually closely related to the number of hotspots because the hotspot regions on the heterostructure aid in incident laser light trapping.[50] The hotspots in ZnO/Ag composites are produced by the gaps between the Ag NPs. In ZnO/Ag1, ZnO/Ag2 and ZnO/Ag3, fewer Ag NPs are anchored on the ZnO FLM and fewer hotspots are formed, resulting in poor SERS enhancement. In ZnO/Ag5, a large amount of Ag NPs agglomerate together, leading to the decrease of the hotspot number and decrease in the SERS activity. ZnO/Ag4 possesses the appropriate amount of Ag NPs, which is favorable for the creation of highly dense hotspots to enhance the Raman intensity. We investigated the role of the heterostructure in the Raman signal enhancement mechanism. Compared to the SERS substrate based on the bare ZnO FLM and pristine Ag NPs, the ZnO/Ag hybrid has a much higher specific surface area, thus allowing for the adsorption of a larger number of target molecules, as well as the high possibility of forming plasmon hotspots. The high sensitivity also resulted from the strong LSPR effect of the Ag NPs and the role of the ZnO–Ag heterojunction. The large SERS enhancement in ZnO/Ag substrates can be primarily ascribed to the strong local electromagnetic effect under a 532 nm laser excitation and resonance coupling between the adjacent Ag NPs anchored on the ZnO surface. The close inter-distance between Ag NPs in the ZnO/Ag composites allows for the formation of hotspots which enhance the excitation light trapping and increase the light interaction with Ag NPs. With increasing Ag amount, the gap distances between adjacent Ag NPs decrease and the electric field intensity increases. ZnO FLM provides a large surface area for loading Ag NPs and the adsorption of MD molecules that cause strong Raman signals in the given excitation area.

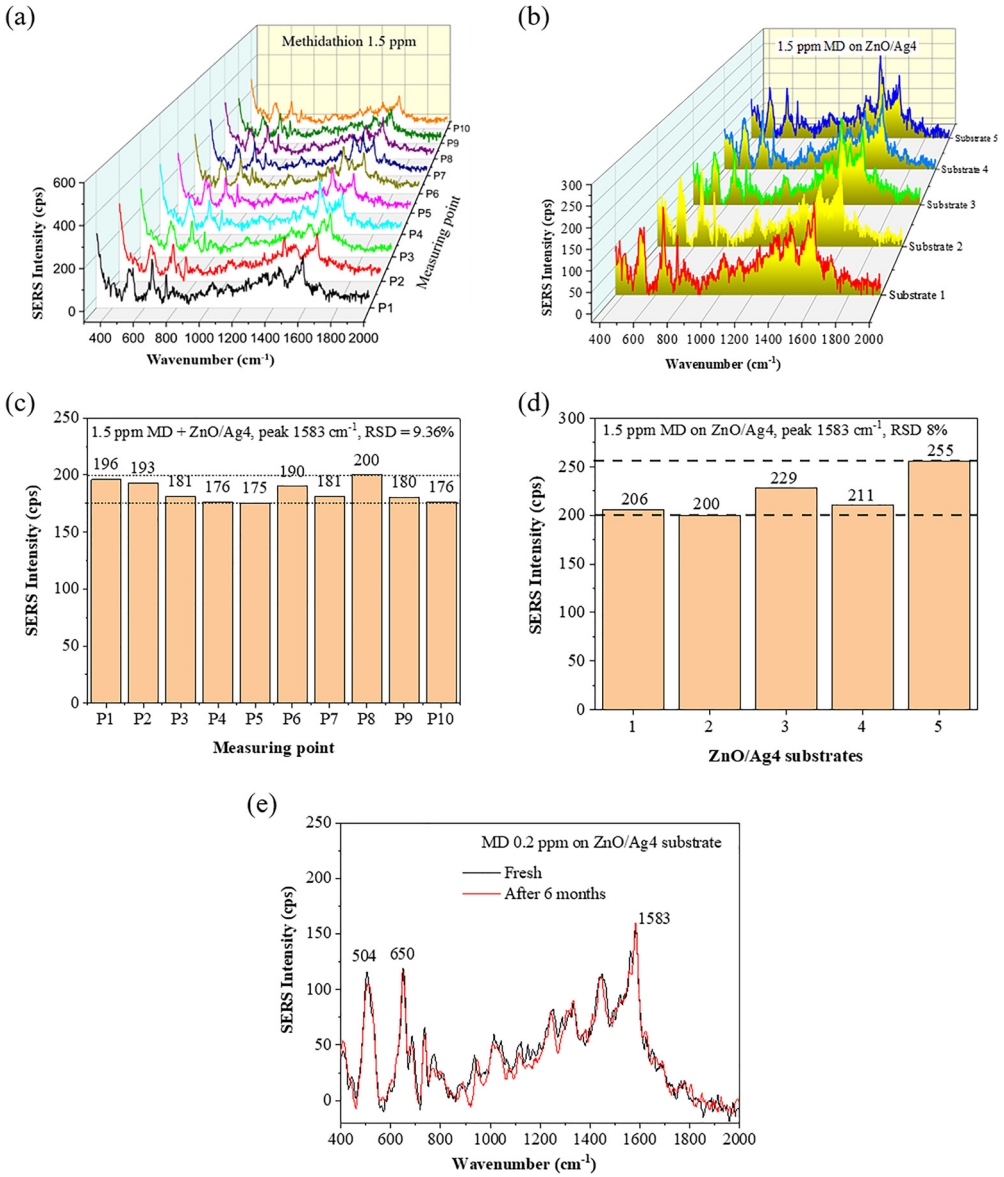


Fig. 9 (a) SERS spectra of MD molecules at a concentration of 1.5 ppm from ten different spots of the ZnO/Ag4 substrate, (b) SERS spectra of MD molecules at a concentration of 1.5 ppm from five independently prepared ZnO/Ag4 substrates, (c) histogram of the peak intensity at 1583 $cm^{-1}$ from (a), (d) histogram of the peak intensity at 1583 $cm^{-1}$ from (b), and (e) stability of the ZnO/Ag4 substrate after 6 months of preservation.

In order to gain further insight on the mechanism of the SERS enhancement, the electromagnetic (EM) enhancement was studied to support the experimental observation. Through finite-difference time-domain (FDTD) simulation, Motla *et al.* studied the electromagnetic field distribution around two Ag NPs when varying the gap between them and found that the electric field intensity decreases with increasing gap, thereby lessening the coupling effect.[9] The electric field intensity reaches the maximum value when the gap between two Ag NPs is zero. In addition, the electric field intensity depends on the size of the Ag NPs. As the size of the Ag NPs increases, the electric field intensity around the nanoparticles increases. The average size of Ag NPs used in this research is 20 nm, which creates the best hotspot regions. Localized hotspots between ZnO and Ag or between Ag and Ag depend on the distance between them.[51] The hotspots are the main contributions to the enhancement in the Raman signal of the analytes. Additionally, the gap between two nearest-neighbor Ag NPs on the ZnO/Ag4 substrate within the range of 50–100 nm is sufficient for MD molecules to enter and contact ZnO and participate in electron transfer during the CT process.

The high-intensity electromagnetic field created between the Ag NPs and the charge transfer (CT) between ZnO/Ag and MD molecules are the main reasons for the SERS enhancement. The experimental results suggested that the excellent SERS activity of the ZnO/Ag hybrid structure may be due to the dense nanogaps forming the hotspots, which increase the electric field around the MD molecules. Additionally, electrons from Ag

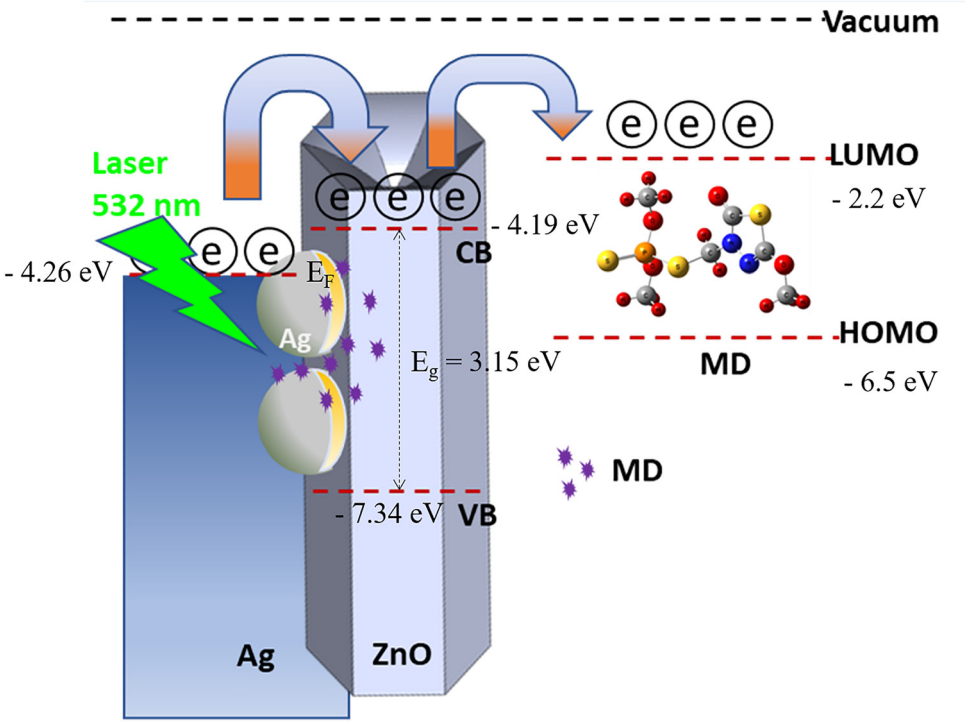


Fig. 10 Schematic of the charge transfer mechanism between the ZnO/Ag and MD molecules under 532 nm laser excitation.

can be transferred to the lowest unoccupied molecular orbital (LUMO) energy level of MD molecules when acted upon by the 532 nm laser. The charge transfer at the semiconductor–probe molecule interface also plays an essential role in improving the SERS signal. The conduction band (CB) of ZnO is above the Fermi energy level of Ag, so electrons excited by LSPR are transferred from Ag to ZnO and then to the LUMO of the MD molecules. The CB of ZnO plays a role as the bridge for electron transfer, enhancing the efficiency of CT (Fig. 10). The work function of ZnO (4.19 eV) is smaller than that of Ag (4.26 eV)[7] and a Schottky barrier is created at the ZnO/Ag interface, which effectively inhibits the recombination of electrons with holes, leading to enhanced local electromagnetic field. The coupling effect between Ag NPs greatly improves the SERS signal of MD.

## 4. Conclusions

In this paper, an efficient SERS substrate based on the ZnO/Ag hybrid heterostructure has been fabricated for the detection of low concentrations of methidathion (MD) pesticide. Spherical Ag nanoparticles, hexagonal ZnO flower-like microrods, and ZnO/Ag composites have been successfully synthesized using the hydrothermal method, followed by reduction reaction. The fabrication method is scalable and low-cost, and does not require sophisticated surface modifications, making it more feasible for field applications. The emergence of a hump at 430–470 nm suggested potential charge transfer characteristics between Ag and ZnO. The SERS substrates exhibit excellent performance in terms of high sensitivity and good uniformity/detection consistency. The ZnO/Ag4 substrate successfully detected the presence of MD molecules at low concentrations with a limit of detection (LOD) of 0.2 ppm and enhancement factor (EF) of $1.1 \times 10^7$. This SERS substrate demonstrated long-term stability after a 6-month period of aging. The simple strategy of submerging the SERS substrate in MD solutions makes the substrate uniform. The good SERS activity can be ascribed to the light trapping mechanism and multiple hotspots of the heterostructure. Thanks to the combined effect of the LSPR of Ag NPs and the charge transfer mechanism, the ZnO/Ag heterostructure showed good sensitivity towards MD. The coupling effect between Ag NPs and ZnO FLM and the separation between adjacent Ag NPs play an important role in SERS enhancement. DFT calculations showed that the heterostructure increased the hotspot regions on the surface of ZnO FLM/Ag NPs. These results show that the ZnO/Ag can be prepared on a large scale and properly used for the detection of trace amounts of organic and toxic substances like methidathion in fruits, vegetables, or wastewater. Other potential applications of this detection method can be in the areas of food safety, environmental protection, and clinical diagnosis.

## Author contributions

Nguyen Dac Dien and Xuan Hoa Vu: writing the original draft, visualization, validation and reviewing; Thi Thu Ha Pham: writing the original draft, supervision, reviewing, and editing; Ngo Thi Lan, Tran Thu Trang, Pham The Chinh, Truong Xuan Vuong and Thi Thu Thuy Nguyen: conceptualization, methodology; Cao Thanh Hai, Tran Thi Kim Chi, Tran Thi Huong Giang, Pham Thanh Binh, Nguyen Trong Nghia, Nguyen Duc

Toan and Pham Thi Nga: data curation, resources, reviewing and editing.

## Conflicts of interest

The authors declare that they have no known competing financial interests or personal relationships that could have appeared to influence the work reported in this paper.

## Data availability

The datasets used and/or analyzed during the current study are available from the corresponding author upon reasonable request. In addition, all the data generated or analyzed during this study are included in this article.

## Acknowledgements

The authors are grateful to the Vietnam Ministry of Science and Technology for the financial support of ĐT CTVL 2021–2025 under grant number ĐTĐLCN.23/23.

## References

1 C. Cheng, B. Yan, S. M. Wong, X. Li, W. Zhou, T. Yu, Z. Shen, H. Yu and H. J. Fan, *ACS Appl. Mater. Interfaces*, 2010, **2**(7), 1824–1828.
2 C. Li, S. Xu, J. Yu, Z. Li, W. Li, J. Wang, A. Liu, B. Man, S. Yang and C. Zhang, *Nano Energy*, 2021, **81**, 105585.
3 Z. Zhao, Y. Huang, Y. Fan and K. Lai, *Nanomaterials*, 2018, **8**(2), 94.
4 S. K. Vemuri, S. Khanna, S. Paneliya, V. Takhar, R. Banerjee and I. Mukhopadhyay, *Colloids Surf., A*, 2022, **639**, 128336.
5 T. Bora, *Recent developments on metal nanoparticles for SERS applications*, IntechOpen, 2018, ch. 6.
6 W. Lv, C. Liu, Y. Ma, X. Wang, J. Luo and W. Ye, *Talanta*, 2019, **204**, 372–378.
7 X. Chen, L. Zhu, Z. Ma, M. Wang, R. Zhao, Y. Zou and Y. Fan, *Nanomaterials*, 2022, **12**(14), 2394.
8 T. T. H. Pham, X. H. Vu, N. D. Dien, T. T. Trang, T. T. K. Chi, P. H. Phuong and N. T. Nghia, *RSC Adv.*, 2022, **12**, 7850–7863.
9 A. Motla, D. Sharma, V. R. Soma and S. Annapoorni, *Opt. Mater.*, 2024, **149**, 115110.
10 Q. Tong, W. Wang, Y. Fan and L. Dong, *Trends Anal. Chem.*, 2018, **106**, 246–258.
11 Y. Wu, T. Sun, M. Shao, C. Ji, C. Li, C. Zhang and Z. Li, *Laser Photonics Rev.*, 2025, **19**(4), 2401152.
12 Y. Quan, J. Yao, S. Yang, L. Chen, Y. Liu, J. Lang, H. Zeng, J. Yang and M. Gao, *J. Hazard. Mater.*, 2020, **391**, 122222.
13 T. T. H. Pham, X. H. Vu, N. D. Dien, T. T. Trang, N. Van Hao, N. D. Toan, N. Thi Ha Lien, T. S. Tien, T. T. K. Chi and N. T. Hien, *R. Soc. Open Sci.*, 2023, **10**(5), 221623.
14 T. T. Tran, X. H. Vu, T. L. Ngo, T. T. H. Pham, D. D. Nguyen and V. D. Nguyen, *Phys. Chem. Chem. Phys.*, 2023, **25**(23), 15941–15952.
15 L. Xinao, L. Fengcai, L. Xiu, J. Yang, Z. Xiaofei, L. Zhen, Z. Chao and Y. Jing, *Opto-Electron. Adv.*, 2025, **8**(6), 240260.
16 H. Luo, J. Zhou, H. Zhong, L. Zhou, Z. Jia and X. Tan, *RSC Adv.*, 2016, **6**, 99105–99113.
17 S. Fu, J. Chen, H. Han, W. Wang, H. Shi, J. Fu and Y. Jia, *J. Alloys Compd.*, 2019, **799**, 183–192.
18 L. Yang, X. Jiang, W. Ruan, B. Zhao, W. Xu and J. R. Lombardi, *J. Phys. Chem. C*, 2008, **112**, 20095–20098.
19 S. Hsieh, P.-Y. Lin and L.-Y. Chu, *J. Phys. Chem. C*, 2014, **118**, 12500–12505.
20 Y. Shang, X. Zhang, X. Wang, J. Yang, X. Shi, L.-L. Qu and Y. Gu, *Mater. Sci. Eng. B*, 2025, **320**, 118396.
21 T. Jiao, F. Y. H. Kutsanedzie, J. Xu, A. Viswadevarayalu, M. M. Hassan, H. Li, Y. Xu and Q. Chen, *Phys. Lett. A*, 2019, **383**(12), 1312–1317.
22 Q. Sun, Q. Y. Zhang, N. Zhou, L. Y. Zhang, Q. Hu and C. Y. Ma, *Appl. Surf. Sci.*, 2021, **565**, 150524.
23 J. Yang, B. Chen, J. Peng, B. Huang, W. Deng, W. Xie and Z. Luo, *Plasmon.*, 2021, **16**, 1059–1070.
24 T. Zhu, H. Wang, L. Zang, S. Jin, S. Guo, E. Park, Z. Mao and Y. M. Jung, *Molecules*, 2020, **25**(5), 1199.
25 N. D. Dien, *Adv. Mater. Sci.*, 2019, **4**, 1–5.
26 T. Dong, Y. Wu and M. Mei, *Opt. Mater.*, 2024, **152**, 115405.
27 W. Deng, L. Yuan, P. Wan, J. Sun, C. Kan, D. Shi, C. Xu and J. Lu, *Nano Energy*, 2025, **133**, 110449.
28 K. Ramachandran, A. Hamdi, S. Columbus, N. Al Meselmene, E. Dogheche, K. Daoudi and M. Gaidi, *Surf. Interfaces*, 2022, **35**, 102407.
29 X. Wang, X. Zhu, Y. Tao, E. Zhang and X. Ren, *Spectrochim. Acta, Part A*, 2023, **290**, 122277.
30 A. Güngördü, *Aquat. Toxicol.*, 2013, **140–141**, 220–228.
31 C. Li, H. Zhu, C. Li, H. Qian, W. Yao and Y. Guo, *Food Chem.*, 2021, **354**, 129552.
32 C. S. Vareli, I. R. Pizzutti, L. Gebler, C. D. Cardoso, M. E. Z. Fontana, B. Reichert and B. D. Jänisch, *Anal. Methods*, 2019, **11**(42), 5455–5463.
33 T. Bedassa, A. Gure and N. Megersa, *Food Anal. Methods*, 2015, **8**, 2020–2027.
34 X. Dou, X. Chu, W. Kong, Y. Yang and M. Yang, *RSC Adv.*, 2015, **5**(105), 86163–86171.
35 Q. Yang, Q. Li, H. Li and F. Li, *J. Agric. Food Chem.*, 2021, **69**(9), 2689–2696.
36 Q. Li, J. Wu, Q. Yang, H. Li and F. Li, *Anal. Chem.*, 2021, **93**(19), 7362–7368.
37 T. Itoh and Y. S. Yamamoto, *Nanoscale*, 2021, **13**(3), 1566–1580.
38 X. Luo, R. Pan, M. Cai, W. Liu, C. Chen, G. Jiang, X. Hu, H. Zhang and M. Zhong, *Sens. Actuators, B*, 2021, **326**, 128826.
39 Y. Zhang, S. Zhao, J. Zheng and L. He, *Trends Anal. Chem.*, 2017, **90**, 1–13.
40 G. Lin, J. Zhu, M. Wu, P. Lu and W. Wu, *AIP Adv.*, 2019, **9**(3), 035203.

41 C. Yao, F. Cheng, C. Wang, Y. Wang, X. Guo, Z. Gong, M. Fan and Z. Zhang, *Anal. Methods*, 2013, **5**(20), 5560–5564.
42 C. Wang, K. W. Wong, Q. Wang, Y. Zhou, C. Tang, M. Fan, J. Mei and W.-M. Lau, *Talanta*, 2019, **191**, 241–247.
43 Y. Chen, H. Liu, X. Li, S. Tang, C. Gu, G. Wei, T. Jiang and X. Zhou, *Sens. Actuators, B*, 2021, **339**, 129856.
44 G. Nagaraju, Udayabhanu, Shivaraj, S. A. Prashanth, M. Shastri, K. V. Yathish, C. Anupama and D. Rangappa, *Mater. Res. Bull.*, 2017, **94**, 54–63.
45 Y. Gui, S. Zhao, K. Tian, J. Wu, H. Guo, X. Qin, X. Qin, D. Guo and C. Fang, *Micro Nanostruct.*, 2024, **196**, 207984.
46 S. Lei, C. Tao, J. Li, X. Zhao and W. Wang, *Appl. Surf. Sci.*, 2018, **452**, 148–154.
47 J. Tauc, *Optical properties of amorphous semiconductors*, Plenum Publishing Company Ltd., 1974.
48 Samriti, P. Kumar, A. Y. Kuznetsov, H. C. Swart and J. Prakash, *ACS Mater. Au*, 2024, **4**, 413–423.
49 X.-X. Huang, F. Yuan-Chao, C. Shi-Liang, C. Xiao-Jing, A. Shujat, C. Xi, Y. Lei-Ming, S. Wen, C.-X. Jiang and G.-Z. Huang, *Chin. J. Anal. Chem.*, 2022, **50**(7), 100107.
50 T.-H. Chang, K.-W. Chuang and Y.-C. Chang, *J. Alloys Compd.*, 2022, **893**, 162288.
51 R. Li, C. Han and Q.-W. Chen, *RSC Adv.*, 2013, **3**, 11715–11722.